Article:
Shi, Y., Wang, J.B. and Wang, B. (2021) Transient 3D lumped parameter and 3D FE thermal models of a PMASynRM under fault conditions with asymmetric temperature distribution. IEEE Transactions on Industrial Electronics, 68 (6). pp. 4623-4633. ISSN: 0278-0046

https://doi.org/10.1109/tie.2020.2988224

Transient 3D Lumped Parameter and 3D FE Thermal Models of a PMASynRM under Fault Conditions with Asymmetric Temperature Distribution

Yanwen Shi, Jiabin Wang, *Senior Member,* and Bo Wang, *Member IEEE*

Post Conference Paper

***Abstract*— This paper proposes a novel transient 3D lumped-parameter (LP) thermal model and a 3D finite-element (FE) thermal model of a triple redundant 9-phase permanent magnet-assisted synchronous reluctance machine to predict the asymmetric temperature distribution under various fault conditions. Firstly, the predicted transient and steady-state temperatures are compared between the 3D LP and the 3D FE thermal models under fault conditions with uneven loss distribution. Also, the temperatures predicted by the LP and FE thermal models which account a number of practical issues are comprehensively compared with the test results under healthy and short-circuit fault conditions. The relative merits of the two thermal models are discussed. It is shown that both models have reasonable accuracy in predicting the machine thermal behavior under fault conditions and can be chosen according to the requirements.**

***Index Terms*— Permanent magnet-assisted synchronous reluctance motor, lumped-parameter thermal model, 3D FE thermal model, fault tolerant, asymmetric temperature distribution.**

I. INTRODUCTION

Air traffic has gained a worldwide growth in popularity in a last few decades. In order to offer improved performance, fuel economy and environmental sustainability, fault tolerant machines for safety critical applications in "more electric aircraft" and "all electric aircraft" technologies are extensively investigated. The most important requirement of the fault tolerant machine is its ability to manage and mitigate faults. It has been reported that winding failure resulting from insulation break-down is one of the dominant failure modes within the machine. Since insulation life decreases significantly when winding temperature increases, temperature is one of the key limiting factors for fault tolerant machines. Therefore, accurately predicting the temperature distribution and hotspot temperature under various conditions, especially some typical fault conditions, is vital at design stage.

Among all the common faults, inter-turn short circuit (SC) fault is one of the leading causes of winding failures and it is particularly critical since only a few turns are in the short-circuit path[1]. Consequently, the significant fault current several times greater than rated may give rise to a local hotspot and ultimately cause a complete insulation failure of the winding. It is important to quantify the rate of temperature rise and the permissible maximum time duration in which the fault should be detected and an appropriate mitigation action is taken before causing further damage. Usually for the triple redundant fault tolerant machine under study, terminal SC is applied on the faulted 3-phase as a fault mitigation measure upon detection of an inter-turn SC fault. Thus, thermal modelling and analysis of these two fault conditions are the main focus in this paper.

There has been extensive research on the thermal analysis under healthy condition by LP thermal model, FE analysis or electromagnetic (EM) thermal coupled simulation [2-8]. Few papers have considered the thermal analysis by LP and FE thermal models under fault conditions with asymmetric temperature distribution. A steady state LP thermal model is employed in [9] to evaluate temperatures of machine components under terminal SC faults by accounting non-uniform copper loss distribution. Similarly, a reduced LP thermal model is reported in [10] to facilitate fault diagnosis of winding open-circuit or an inter-turn SC fault in a DC motor by inputting varying copper losses to different winding nodes. However, in this LP model, the field winding containing an inter-turn SC fault only has one node which cannot differentiate the temperatures in fault turns and healthy turns. A LP thermal network dividing the fault phase into healthy and fault turns is presented in [11] in order to estimate the resistance for an inter-turn fault detection in permanent magnet synchronous machine. However, not only the discretization levels of all above LP models are insufficient, but also these models fail to consider circumferential heat transfer among stator which may have large effect on final temperature distribution. A steady-state LP model with high discretization level and considering circumferential heat transfer has been established in [12]. Alternatively, 3D FE model is often employed for thermal analysis under fault conditions. For example, a 3D thermal model is adopted in [9] to predict temperatures under terminal SC faults, and a similar approach is employed in [13] to evaluate uneven temperature distribution under different open-circuit faults. It should be noted, however, that the 3D FE approach is very time-consuming, and it cannot be practically employed at design optimization stage of fault-tolerant machines for which thermal behaviors under various fault

condition need to be carefully assessed.

In general, it is important to have a computationally efficient thermal model with high discretization level and the capability of considering practical issues to predict the asymmetric temperature distribution of fault tolerant machines under common fault conditions, especially for inter-turn SC and terminal SC faults. However, systematic approaches are currently rare.

This paper will establish a novel transient 3D LP thermal model and a 3D FE thermal model for thermal analysis under fault conditions of a triple redundant, 9-phase permanent magnet-assisted synchronous reluctance motor (PMASynRM). The LP thermal model is built in Matlab Simulink and the FE thermal model is built in JMAG. Both two models are established with high discretization level and with the capability of predicting temperatures under faults by considering circumferential heat transfer, uneven loss distribution, and variable copper loss as well as variable thermal properties of coolant fluid with temperature. The detailed modelling of the transient LP and FE thermal models with all the thermal parameters are described. Subsequently the temperatures predicted by the two models under the same fault conditions with uneven loss distribution will be compared. Moreover, the transient and steady-state temperatures predicted by the 3D LP and 3D FE thermal models considering more realistic issues will be comprehensively compared with the experimental results under healthy and SC fault conditions. The merits of the two thermal models are also assessed.

II. 9-PHASE (3X3-PHASE) PMASYNRM

Figure 1 shows a fault tolerant triple redundant, 9-phase (3x3-phase) PMASynRM reported in [1]. Table I presents the main geometry parameters of the machine. The PMASynRM has inherently large reluctance torque, leading to comparable performance with conventional PM machines in terms of efficiency and torque density. Additionally, the high saliency of the machine results in the low PM usage which leads to the low back-EMF and low SC current to improve the fault tolerance. Moreover, from Fig. 1 (b), this machine employs three separated 3-phase windings, denoted as ABC, DEF and GHI, which do not overlap with each other compared with the conventional overlapped distributed windings. This winding layout improves the physical and thermal isolations between the different 3-phase sets. Apart from that, each 3-phase set is controlled by an independent 3-phase inverter for electrical isolation. Thus, fault propagation between different 3-phase winding sets is minimized and the machine has excellent fault tolerant capability under many common faults [1, 14].

Since an inter-turn SC with the least number of SC turns, i.e., one turn, leads to the highest SC current and most rapid temperature rise in the faulted region, the thermal models described in this paper focus on the prediction of the thermal behaviors of this machine under one turn SC and one turn SC with 3-phase terminal SC as a mitigation measure. This knowledge is important to ensure fault tolerant ability of the machine in the worst case because experimental measurements of the hotspot temperature in such conditions are not always possible. However, the techniques described in the paper are applicable to assessing asymmetric temperature distribution in any fault conditions.

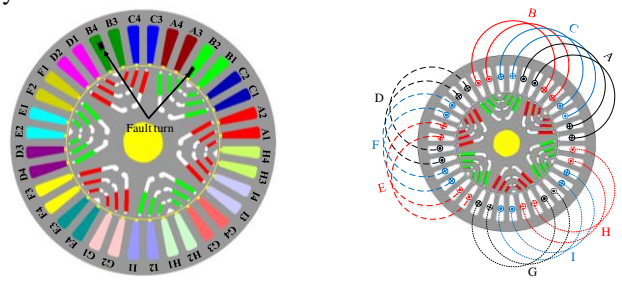

Fig. 1. Cross section of a triple redundant, 9-phase PMASynRM. (a) Named slots and short-circuit turn. (b) Layout of windings.

TABLE I. MAIN GEOMETRY PARAMETERS.

Parameters	Value
Axial stack length	110mm
Stator radius	90mm
Rotor radius	51.75mm
Shaft radius	13.5mm
Airgap thickness	0.75mm
Slot depth	27.55mm
Tooth width	5.1mm

Without loss of generality, it is assumed that the worst case one turn SC occurs in phase B and terminal SC will be applied to 3-phase set ABC when the fault is detected. The mutual coupling between the two healthy 3-phase sets and the faulty 3-phase set will result in a magneto-motive force (MMF) offset component in the region occupied by 3-phase set ABC [15]. Therefore, the location of the SC turn will affect the flux linkage and consequently the circulating current and resultant copper loss. It has been shown in [16] that when the SC turn is located at the two black quadrangles shown in Fig. 1 (a) of slots B2 and B4, the SC current and copper loss are the highest. The subsequent analysis is focused on this worst case.

III. LUMPED PARAMETER THERMAL MODEL

For derivation of the 3D LP thermal model of the 36-slot PMASynRM with inter-turn SC fault, some assumptions are made. Firstly, the thermal dissipation in the rotor part is mainly in the radial direction while the thermal dissipation in the winding area considers the radial, axial and circumferential directions. Additionally, the thermal dissipation in the stator core is not only in the radial direction but also in the circumferential direction via the stator teeth because of the large uneven loss distribution. The commercial software package, such as Motor-CAD [17] as well as empirical equations presented in [3], are used to determine critical parameters and help develop the model.

The winding region is of great thermal significance and has to be analyzed with care, especially under SC fault conditions, because it has high copper loss and great heat intensity. The winding usually consists of conductors, wire insulations and impregnations, so the equivalent thermal conductivity based on analytical homogenization [18-19] is employed. It is worth noting that the axial thermal conductivity of windings is commonly far larger than the cross-sectional thermal conductivity.

The winding is assumed that only contains two materials as the volume of the wire insulation is much smaller than that of the impregnation. The Hashin and Shtrickman approximation [18] can be used to estimate the radial/circumferential equivalent thermal conductivity $k_{rad/cir}$ in (1):

$$k_{rad/cir} = k_p \frac{(1+v_c)k_c + (1-v_c)k_p}{(1-v_c)k_c + (1+v_c)k_p} \quad (1)$$

where k_c and k_p are the copper and impregnation thermal conductivity, respectively; v_c is the copper slot fill factor.

The axial equivalent thermal conductivity k_{axial} is simply calculated from the parallel model [19] for the two materials and is given by:

$$k_{axial} = v_c k_c + (1-v_c)k_p \quad (2)$$

The equivalent conductivities in (1) and (2) for multi-strand windings with impregnation have been validated by experiments reported in [19-20].

The equivalent mass density ρ_e and specific heat capacity c_e of the winding also combine the effect of conductors and impregnations as given by [19]:

$$\rho_e = v_c \rho_c + (1-v_c)\rho_p \quad (3)$$

$$c_e = \left[v_c \rho_c c_c + (1-v_c)\rho_p c_p \right] / \rho_e \quad (4)$$

where c_c and c_p are the specific heat capacity of the copper and impregnation, respectively; ρ_c and ρ_p are the mass density of copper and impregnation, respectively.

Figure 2 shows the scehmatic of a half slot-tooth region with key dimensions indicated. Figure 3 shows the LP thermal model of a healthy slot-tooth region.

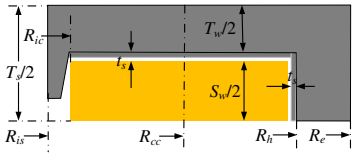

Fig. 2. The schematic of a half slot-tooth region.

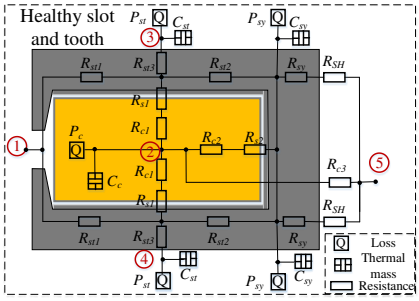

Fig. 3. LP thermal model of the healthy slot-tooth region.

It can be seen that the thermal resistance of the winding is divided into the active part R_{c1}, R_{c2} and the end-winding part R_{c3}. Part of the heat in the winding is transferred to the stator tooth via R_{c1} and slot liner R_{s1}, and to the stator yoke via R_{c2} and slot liner R_{s2}. Additionally, since the potted end winding is in direct contact with the housing, part of the heat in the winding is transferred through the end winding R_{c3} to the housing directly. In contrast, the heat in the stator core can not only be dissipated radially through the tooth part R_{st1}, R_{st2}, and the yoke part R_{sy} to housing via the contact thermal resistance R_{SH} between stator and housing, but also circumferentially through tooth part R_{st3} to the adjacent tooth. All the thermal resistances and capacitances can be derived using the governing principle of the heat conduction [4], and they are given in (5) to (14) and in (15) to (17), respectively.

$$R_{c1} = S_w / \left[4k_{rad/cir} L_A (R_h - R_{ic}) \right] \quad (5)$$

$$R_{c2} = \left(R_h - R_{cc} \right) / \left(k_{rad/cir} L_A S_w \right) \quad (6)$$

$$R_{c3} = \frac{L_A + L_{edw}}{8k_{axial} S_w (R_h - R_{ic})} + \frac{\ln(R_e / R_{cc})}{4k_{rad/cir} L_{edw} (\pi / N_s)} \quad (7)$$

$$R_{s1} = t_s / \left[k_r L_A (R_h - R_{is}) \right] \quad (8)$$

$$R_{s2} = t_s / \left(k_r L_A S_w \right) \quad (9)$$

$$R_{st1} = 2\left(R_{cc} - R_{is} \right) / \left(k_{stator} L_A T \right) \quad (10)$$

$$R_{st2} = 2\left(R_h - R_{cc} \right) / \left(k_{stator} L_A T \right) \quad (11)$$

$$R_{st3} = T_w / \left[4k_{stator} L_A (R_h - R_{is}) \right] \quad (12)$$

$$R_{sy} = N_s \ln(R_e / R_h) / \left(\pi k_{stator} L_A \right) \quad (13)$$

$$R_{SH} = N_s t_{sh} / \left(\pi k_{sh} L_A R_e \right) \quad (14)$$

where L_A is the length of the active winding; L_{edw} is the length of the end winding of a quarter turn; k_{stator}, k_r and k_{sh} are the thermal conductivities of the stator core, slot liner and interface between the stator and housing, respectively; N_s is the slot number; t_{sh} is the contact thickness between the stator and housing. All the other dimensional parameters are illustrated in Fig. 2. It is obvious that R_{c3} contains two components representing the cross-sectional heat transfer in the end winding part and axial heat transfer in the whole winding part. The stator iron loss is separated into the loss in tooth region, P_{st}, and the loss in yoke, P_{sy}, while the stator core capacitance is similarly separated into C_{st} and C_{sy}, which are inputted to the stator tooth and yoke nodes, respectively. In healthy slots, the winding temperature is represented by that in one node to which the copper loss P_c and winding thermal capacitance C_c are connected. The thermal capacitances are given in (15) – (17).

$$C_{st} = (R_h - R_{is}) L_A (T_w / 2) \rho_{stator} c_{stator} \quad (15)$$

$$C_{sy} = (\pi / N_s)(R_e^2 - R_h^2) L_A \rho_{stator} c_{stator} \quad (16)$$

$$C_c = [(R_h - R_{ic}) L_A S_w + (2\pi / N_s)(R_e^2 - R_{is}^2) L_{edw}] \rho_e c_e \quad (17)$$

where c_{stator} and ρ_{stator} are the heat capacity and mass density of the stator core, respectively.

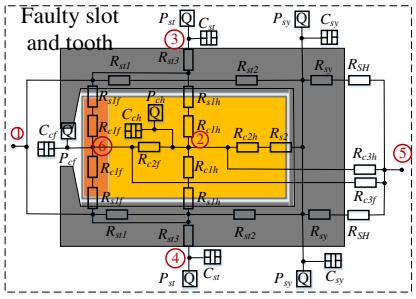

Fig. 4. LP thermal model of the fault slot-tooth region with inter-turn SC.

Figure 4 shows the LP thermal model of the fault slot-tooth region containing inter-turn SC. Compared with Fig. 3, the winding is divided into healthy part and fault part. Thus, the

thermal resistances R_{c1}, R_{c2}, R_{c3} and R_{s1}, and the thermal capacitance C_c are also divided into two parts and the values in each part are determined by the associated number of turns. Likewise, the copper losses of the SC turn P_{cf} and the healthy part P_{ch} are inputted to the two associated nodes.

Two thermal networks in Figs.3 and 4 form the building blocks for the LP model of the machine. The slots B2 and B4 with inter-turn fault are illustrated in Fig. 4, while the rest slots are seen in Fig. 3. Figure 5 (a) shows the LP thermal model of the stator containing all the slots, in which the building block for each slot is identified by the slot name with the numbered nodes for connection to other parts of the stator. Node 3 in each stator slot model is connected to node 4 of the adjacent slot model for the thermal dissipation in the circumferential direction. The inner bore of the stator is in contact with the airgap. The heat transfer between the total winding and the airgap or the end cap air is represented by the thermal resistance R_{ca} for healthy slots and by R_{cah} and R_{caf} for the fault slots.

Figure 5 (b) presents the LP thermal model of the rotor, concluding shaft, rotor and magnet. The rotor iron loss is divided into yoke and iron-rib parts, and the eddy current loss in magnets is inputted into the magnet node. Furthermore, convective heat transfer at the end region of the shaft, rotor and magnet with the end cap air is also accounted by three thermal resistances shown in Fig. 5 (b). The thermal resistances and capacitances of the shaft, rotor yoke, magnets and rotor iron-ribs as well as the thermal contact resistance between the magnet and rotor are calculated by the same method for the stator described previously.

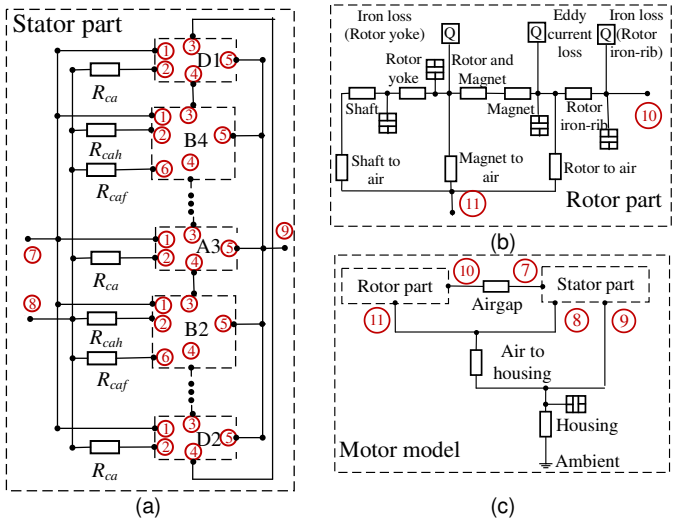

Fig. 5. LP thermal model of a 36-slot PMASynRM with inter-turn SC. (a) Stator part. (b) Rotor part. (c) Motor model.

Figure 5 (c) shows the LP thermal model of the whole motor, in which the rotor part and stator part represented by their block names are connected by the thermal resistance of the airgap and the thermal resistance between the air in the rotor end region and the stator housing. Internal convection resistances, such as the shaft, magnet, rotor, winding to the housing via end cap air are estimated by Motor-CAD[17]. The convective resistances between the rotor and airgap as well as between the stator and airgap can be obtained by the method in [12] or also from Motor-CAD. They are similar.

As the housing has the oil cooling jacket, the machine is mainly cooled by the oil circulation. Thus, the housing thermal resistance combines the housing conduction resistance and the convection resistance of the cooling system. Further, the ambient temperature is set as the oil temperature. The 3D LP model is built in Matlab Simulink.

IV. 3D FE Thermal Model

The 3D FE thermal model is shown in Fig. 6 where different components are indicated. Figure 6 (a) shows the 1/3 FE model encompassing 12 slots and half of the machine axial length, while Fig. 6 (b) shows the winding part of the full 3D FE thermal model containing 36 slots and half the axial length. The full FE thermal model is more accurate than the 1/3 model for thermal analysis when the heating effect and temperature distribution in the three 3-phase winding sets are quite asymmetric, such as those under one turn SC with or without 3-phase terminal SC. By contrast, the 1/3 model may be adopted when the machine is healthy or when the heating effect of the fault is localized and is less significant compared to the total of the machine under a given load condition, or over a short duration in which the heat is more likely to be stored in the materials than dissipate to other regions. It has advantages of smaller size and computationally less demanding with reasonable accuracy.

From Fig. 1, the end winding layout is quite complex to represent in the 3D FE model. Further, because the copper loss and temperature distribution in the healthy and faulted turns are different, the end winding part cannot be simplified as a homogeneous ring. Thus, the end winding is simplified in the FE thermal model as straight winding segments with the same equivalent length as those in the prototype machine as in Fig. 6. The 3D FE thermal model is built according to [12] in JMAG [21]. The schematic diagram of heat equivalent circuit shown in Fig. 7 explains the heat transfer network of the 3D thermal model of this motor. Additionally, the windings are potted and composed of conductor and Stycast 2676FT. The thermal coupling between two different phases in the end winding is transferred by covered potting.

The heat conductions and thermal mass are accounted automatically in the 3D FE thermal model when the thermal conductivities and heat capacities of various components are appropriately set, such as potting, winding, stator core, rotor core, magnets and shaft, etc. The equivalent radial/circumferential and axial conductivities in (1) and (2), and the equivalent heat capacity in (4) of the winding are also used in the 3D model.

The slot liners and thermal contact resistances between two constituent regions, such as the magnet and rotor core, are modelled in the 3D thermal model by setting appropriate gap thickness and the thermal conductivity of the interface materials.

All the internal convection thermal resistances between the various parts and air have been obtained in the LP thermal model. The heat convection coefficient of a surface can be calculated when its area is known in the 3D model. These

values are used for setting up convection boundary conditions in the 3D thermal model.

The oil cooling jacket can be represented as a temperature boundary with a thermal convection resistance between the stator cooling channels and cooling oil in the 3D thermal model [22] shown in Fig. 7. The housing is not built in the FE model as in Fig. 6. However, the conduction resistance and capacitance of the housing, the thermal contact resistance between the stator core and housing, and the convection thermal resistance between the end cap air and the housing are inputted in the integrated circuit with the FE model.

The insulation paper and the glue are neglected in both LP and 3D FE thermal models for simplification which may lead to inaccuracy of the results. Moreover, the temperature coefficients of the thermal conductivities of the core material, shaft, copper, and housing are negligible. Therefore, the thermal conduction resistances of different components keep same during thermal analysis.

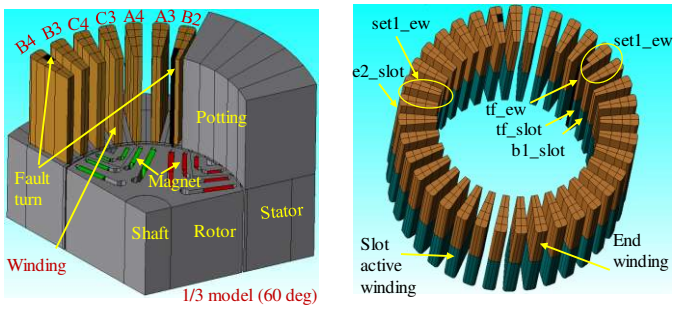

Fig. 6. FE thermal model. (a) 1/3 model. (b) Winding part of the whole model.

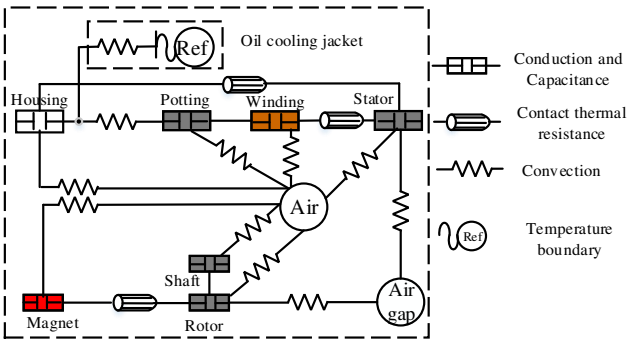

Fig. 7. Schematic diagram of heat equivalent circuit of this motor.

V. Comparison of LP and FE Thermal Models

The 3D LP model and the full 3D FE model as shown in Fig. 6 (b) have been used to predict the transient thermal behavior of the PMASynRM under F1 which is one turn SC and F2 which is one turn SC with 3-phase terminal SC conditions when the machine operates at 4000 rpm with the rated current of 120A excited in the health phases. Both of these two models contain 36 slots. Under one turn SC, only slots B2 and B4 have inter-turn fault while other slots are healthy in the 3D LP model. Moreover, under one turn SC with 3-phase terminal SC, slots B2 and B4 have inter-turn fault, slots of 3-phase set ABC have terminal SC faults while the rest slots are healthy in the 3D LP model.

The eddy current is induced in PM magnets with the material of VACOMAX 225 HR and causes eddy current loss. The iron loss is dependent on the geometry dimension and flux distribution. The iron loss P_{fe} includes hysteresis loss P_h, classical eddy current loss P_e and excess eddy current loss P_x, and can be predicted by FE method based on Bertottie loss model as in (18). Where f is the frequency; B is the flux density; k_f is the stack packing factor; k_h and k_e are hysteresis and excess loss coefficient, respectively; σ is the core material conductivity; d is the thickness of the lamination.

$$P_{fe} = P_h + P_e + P_x$$
$$P_{fe} = k_f \int \left(k_h f B^2 + \frac{\sigma d^2}{12}\left(\frac{dB}{dt}\right)^2 + k_e \left(\frac{dB}{dt}\right)^{1.5} \right) \quad (18)$$

The copper loss is determined by the winding resistance and the square of current. The eddy current losses in the magnets calculated by FE method are 27.9W and 23.7W under F1 and F2, respectively. The calculated iron losses are 307W and 221.4W under F1 and F2, respectively. The initial copper losses at 20°C are 1671W and 1043W under F1 and F2, respectively. The mechanical loss including the windage and the bearing loss is estimated from the machine with similar dimensions as in [20]. At the rated speed, the mechanical loss is about 15W and makes up lower than 1.2% of the total loss. Therefore, the mechanical loss is neglected both in the LP and FE models. As the eddy current loss in the magnets only accounts for smaller than 2% of the total loss. The hysteresis loss dominating the iron loss (73%) at the operating speed does not vary essentially with the temperature [23]. Thus, the iron loss and eddy current loss are considered independent of temperature. However, the copper loss variation with temperature is accounted through iteration until convergence with the predicted temperature.

Moreover, it can be seen from the winding layout in Fig. 1 (b) that the middle part of the slots in a 3-phase winding has more number of overlapped end winding segments than the two sides. To represent the uneven distribution of the copper loss in the end winding region, the copper loss density in the end winding conductors associated with different slots is set proportional to the number of overlapped end winding segments over the slot. For example, the end winding of slot B4 has one overlapped segment while that of B2 has six. Hence, the copper loss density in the former is 6 times lower than that of the latter. Obviously, it is easy to quantify the uneven distribution of the copper loss in the end winding region of the 3D FE thermal model. However, in the 3D LP model, as the active winding and the end winding are connected to one node, the total loss of the whole winding per slot with uneven loss distribution is inputted and the average temperature of the slot is extracted from this node.

The steady-state average temperatures of different parts, such as the rotor, magnet, stator tooth, stator yoke, winding, the healthy part of slot B2 (B2_healthy) and slot B4 (B4_ healthy), the SC turn of slot B2 (B2_fault) and slot B4 (B4_fault) are extracted and compared. The comparisons of temperatures under one turn SC and one turn SC with 3-phase terminal SC

predicted by the two models are given in Table II and Table III, respectively. It can be seen that the differences predicted by the two models under one turn SC with 3-phase terminal SC are smaller than those under one turn SC. However, all the temperature differences are within ±14ºC. It is seen that the 3D LP model is sufficiently accurate to predict temperatures under fault conditions, even to predict the temperature of the fault turn. Moreover, the temperatures of slot B2 are much larger than those of slot B4 due to the fact that the copper loss assigned to the end-winding segments of each coil is different as explained above.

TABLE II. COMPARISONS OF TEMPERATURES UNDER ONE TURN SC

Component	LP thermal (°C)	FE thermal (°C)	Difference (°C)
Rotor	138	140	-2
Magnet	139	140	-1
Stator tooth	114	121	-7
Stator yoke	95	93	2
Winding	120	128	-8
B2_healthy	208	221	-13
B2_fault	394	380	14
B4_ healthy	156	162	-5
B4_fault	209	202	7

TABLE III. COMPARISONS OF TEMPERATURES UNDER ONE TURN SC FAULT WHEN 3-PHASE TERMINAL SC IS APPLIED FOR FAULT MITIGATION

Component	LP thermal (°C)	FE thermal (°C)	Difference (°C)
Rotor	110	112	-2
Magnet	111	113	-2
Stator tooth	89	96	-7
Stator yoke	77	80	-4
Winding	88	91	-2
B2_healthy	96	89	7
B2_fault	110	105	5
B4_healthy	88	85	3
B4_fault	90	86	4

The transient temperatures of the rotor, magnet, stator, B2_fault and B4_fault predicted by the LP and FE thermal models under one turn SC fault are compared in Fig. 8. It can be concluded that the transient and steady-state results predicted by the two models match well. It can be seen that the average temperature of the fault turn in slot B2 under one turn SC condition predicted by both two models reaches over 380ºC. The machine will be completely damaged if the fault is not dealt with in a timely manner. In contrast, by application of terminal SC of the faulty 3-phase through inverter once the fault is detected, the average temperature is managed below 110ºC. The machine drive can continue to operate albeit the torque capability is reduced to ~2/3.

The 3D FE thermal model needs 2Gb memory and 18 minutes to compute while the 3D LP thermal model requires 25 times less memory and can be solved 12 times faster. The LP model shows good accuracy for predicting the transient and steady-state temperature distribution under fault conditions. The FE model can provide more detailed temperature distribution with better accuracy.

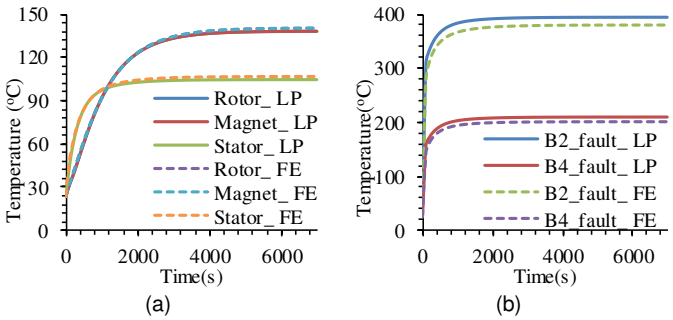

Fig. 8. Transient temperatures between LP and FE models under one turn SC. (a) Transient temperature comparisons of the rotor, magnet and stator. (b) Transient temperature comparisons of B2_fault and B4_fault.

VI. COMPARISON OF PREDICTIONS BY LP AND FE THERMAL MODELS WITH MEASUREMENTS

A prototype PMASynRM has been built. Two extra terminals for the turn B_f are added in phase B2 coil as in Fig. 9 (a) and brought out from the winding by two thick fault-emulation cables as shown in Fig. 9 (b). Besides, the fault-emulation cables are connected to a high current relay shown in Fig. 9 (c) to control fault injection and removal during experiments. The 3-phase terminal SC is applied through the 3-phase inverter by setting the voltage demand to zero.

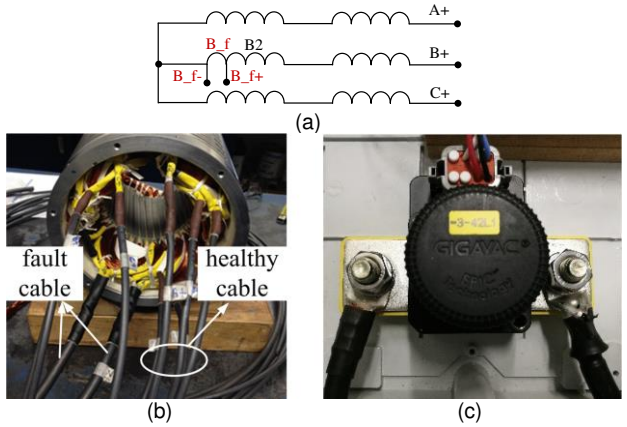

Fig. 9. Motor winding leads and relay for turn fault. (a) The terminal connection of set ABC. (b) Leads. (c) Relay.

The prototype PMASynRM is mounted on the test rig shown in Fig. 10 (a). The machine is connected to the AVL dynamometer operated in speed control mode via couplings and inline torque transducer. The machine is driven by a DSP based three 3-phase inverters. Then the prototype employing the oil cooling system is tested for validation of the thermal model. The cooling oil is fed via the inlet and outlet connections as shown in Fig. 10 (c) and circulates in the cooling channel shown in Fig. 10 (b). The inlet and outlet oil temperatures vary from 24ºC to 44ºC and from 25ºC to 57ºC, respectively, during tests due to the limited capacity of the heat exchanger. These variations are measured by two K-type thermocouples and recorded. The coolant volume flow rate is also recorded. Six temperature sensors are placed in the machine windings, three in the end windings and three in slots to measure temperatures in these positions.

To represent the experimental condition, it is necessary to

model the coolant fluid during the tests. Both the 3D LP model and the 3D FE thermal model can cope with these practical issues. Firstly, it has been introduced that the oil cooling jacket could be represented as a temperature boundary with an equivalent convection resistance between the stator cooling channels and cooling oil. In addition, the thermal convection resistance considers the effect of the variable temperature and flowrate on the thermal properties of cooling oil. Moreover, as the inlet, outlet temperatures and the flowrate of cooling oil during operations are variable, the ambient temperature boundary and thermal convection resistance is considered time-dependent in the LP and the FE thermal models. In addition, the FE thermal model can easily extract temperatures of active and end winding regions and compare with the six measured temperatures. However, the LP model could only extract the average temperatures of the whole winding of slots having sensors to compare with six measured temperatures.

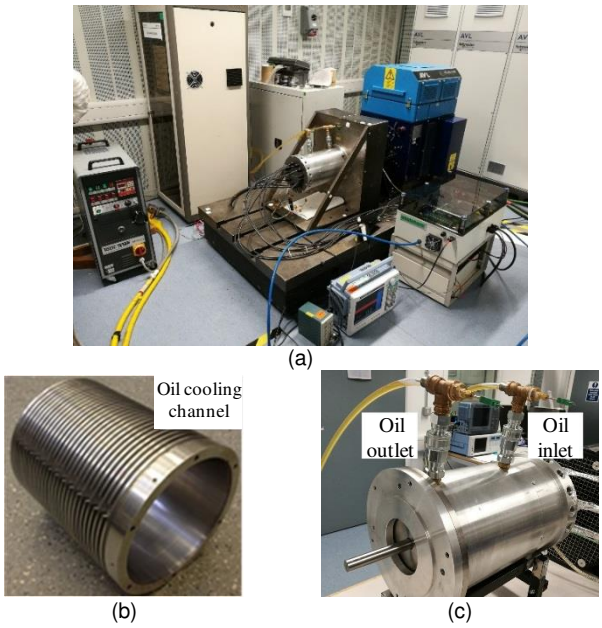

Fig. 10. Prototype on the test rig with oil cooling system. (a) Prototype on the test rig. (b) Cooling jacket. (c) Oil cooling system assembly.

The whole simulation process is divided into a number of steps. In each step, the ambient temperature and the thermal convection resistance of the cooling oil are updated. The temperature distribution extracted from the result file in the previous step is used to calculate new copper loss and set as the initial temperature in the current step.

The prototype is first tested under healthy condition at the base speed of 4000rpm with load current in all phases being set to 80A (2/3 load) for maximum torque per Ampere (MTPA) operation. Since the hotspot temperature under the one turn SC can be extremely high, this fault condition is not tested in order to avoid permanent damage of the prototype. However, the fault conditions of one turn SC when the fault mitigation measure (3-phase terminal SC) is applied are tested at the base speed of 4000rpm with load current in healthy phases being set to 80A and 120A (full load). Each thermal test is performed for 2 hours for reaching steady state. The machine temperatures under these three conditions are predicted by the LP and FE thermal models and the results are compared with the measurements.

A. Healthy Condition at 2/3 Load

As the temperature distribution should be the same in each 3-phase set under healthy condition, the 1/3 3D FE thermal model in Fig. 6 (a) is adopted in simulation.

Under healthy condition at 2/3 load, the eddy current loss in the rotor magnets is 14.7W. The iron loss is 221W, while the initial copper loss at 20ºC is 496W.

The resultant temperature distribution of the winding under the healthy condition at 2/3 load is shown in Fig. 11, where it is evident that the temperatures in the end winding are higher than those in the active winding. Obvious temperature differences in the end windings associated with each coil are seen in Fig. 11. The end winding temperature in the inner middle region is 2~15ºC higher than the rest. This trend is consistent with that observed in the 3D LP model

Among the six temperature sensors, two sensors, denoted as tf_ew and tf_slot, are placed in the end winding and slot regions of the faulted turn in coil B2 as two black cuboid shown in Fig. 6 (b). The two sensors, denoted as b1_slot and e2_slot are placed in the middle of slots of coils B1 and E2, respectively. The other two remaining sensors, denoted as set1_ew and set2_ew are placed in the middle region of the end windings of the ABC and DEF 3-phase sets, respectively, shown in Fig. 6 (b). However, the positions of these sensors are not exact.

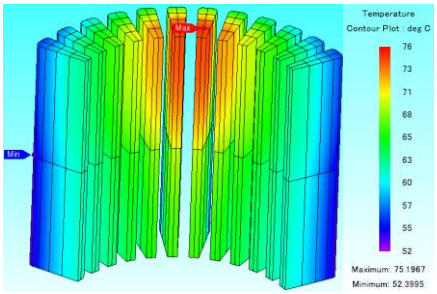

Fig. 11. Temperature distribution under healthy condition at 2/3 load.

The average temperatures of the whole winding of same slots predicted by the 3D LP model, the average temperatures of the same region predicted by the 3D FE thermal model are extracted and compared with the measured results in Table IV. Therefore, it can be observed that the temperatures of the end winding region are similar to those of the active winding region predicted by LP model, while the temperatures of the end winding region are both larger than those of the active winding region predicted by FE model and measured by sensors.

TABLE IV. COMPARISONS OF MEASURED AND PREDICTED AVERAGE TEMPERATURES UNDER HEALTHY CONDITION AT 2/3 LOAD

Temperature (°C)	End winding			Active winding		
	set2_ew	set1_ew	tf_ew	b1_slot	tf_slot	e2_slot
Measured	86	80	78	70	69	71
Predicted FE model	71	71	74	66	71	68
Predicted LP model	66	66	66	65	66	65
Difference FE (%)	-17.4	-11.3	-5.1	-5.7	2.9	-4.2
Difference LP (%)	-23.3	-17.5	-15.4	-7.1	-4.3	-8.5

The differences in percentage of the average temperatures

obtained between FE model and measurements, LP model and measurements are also illustrated in Table IV. It is obvious that the differences between measured temperatures in the active winding regions by sensors b1_slot, tf_slot, e2_slot, and predicted results by FE model and LP model are relatively small, lower than 5.7% and 8.5%, respectively. The differences between measured and predicted temperatures in the end winding region become larger. The largest differences between the measured and predicted results by FE and LP models are 17.4% and 23.3% occurred at set2_ew, respectively. Figure 12 shows the measured and predicted transient temperatures close to sensor tf_slot. It is seen that the measured temperature agrees well with the predicted average temperatures extracted from LP and FE models.

Since the exact positions of the thermal sensors are not known, the minimum and maximum temperatures of the same region predicted by the 3D FE thermal models are extracted and compared with the measured results to give a boundary of possible deviations in Table V. It can be seen that the measured temperatures in the active winding regions are between the minimum and maximum predicted temperatures. The measured temperatures in the end winding regions by sensors set2_ew, set1_ew and tf_ew are higher than the maximum predicted temperatures. The largest difference is 12.8% at set2_ew.

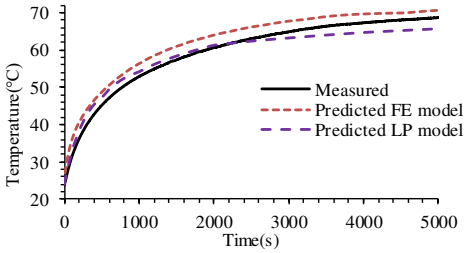

Fig. 12. Comparison of measured and predicted transient temperatures close to sensor tf_slot at 2/3 load.

TABLE V. COMPARISONS OF MEASURED AND PREDICTED TEMPERATURES BY 3D FE MODEL UNDER HEALTHY CONDITION AT 2/3 LOAD

Temperature (°C)	End winding			Active winding		
	set2_ew	set1_ew	tf_ew	b1_slot	tf_slot	e2_slot
Measured	86	80	78	70	69	71
Predicted max	75	75	75	70	72	72
Predicted min	59	59	71	58	67	54
Difference	11	5	3	--	--	--
Difference (%)	12.8	6.3	3.8	--	--	--

B. One Turn SC with 3-phase Terminal SC at 2/3 Load

The prototype has also been tested under one turn SC conditions with 3-phase terminal SC applied to ABC phases at 4000rpm when the current in the healthy DEF and GHI phases is controlled to 80A and 120A.

At one turn SC with 3-phase terminal SC at 2/3 load, the eddy current loss in the rotor magnets is 12.5W. The iron loss is 156.3W, while the initial copper loss at 20°C is 507.5W.

Because the design measures employed for the fault mitigation, the fault current in the SC turn after the mitigation action is 2.7 pu while the RMS phase currents in the ABC phases are quite low. Consequently, total heating effect (loss) in the ABC 3-phase set is 2.2 times lower than that of the other two healthy sets. Because the asymmetric loss distribution, the full 3D FE thermal model in Fig. 6 (b) is adopted for accurate thermal analysis. The predicted temperature distribution presented in Fig. 13 shows that the temperature distributions in the two healthy sets are similar or exhibit 3-phase symmetry and their overall temperature is higher than that of the faulty set which is also observed in the LP model. The hotspot as shown in Fig. 13 is located in the end winding segment of the SC turn due to 2.7 pu current in the faulted turn.

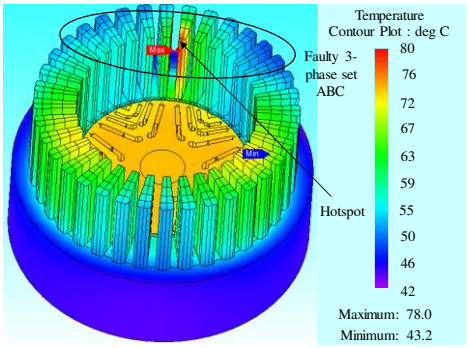

Fig. 13. Temperature distribution under fault condition at 2/3 load.

The average temperatures predicted by the LP and FE thermal models, the minimum and maximum temperatures of the same region predicted by the 3D FE thermal model are extracted and compared with the measured results in Table VI and Table VII, respectively. The differences between the measured and predicted results by FE and LP models are within 11.8% and 14.5%, respectively. In addition, it shows from Table VII that only the measured temperature by sensor set2_ew is larger than the maximum predicted temperature by 6.6%. The five other measured temperatures are between the minimum and maximum predicted temperatures.

TABLE VI. COMPARISONS OF MEASURED AND PREDICTED AVERAGE TEMPERATURES UNDER FAULT CONDITION AT 2/3 LOAD

Temperature (°C)	End winding			Active winding		
	set2_ew	set1_ew	tf_ew	b1_slot	tf_slot	e2_slot
Measured	76	63	66	54	62	63
Predicted FE model	67	57	72	56	68	63
Predicted LP model	65	56	70	58	70	65
Difference FE (%)	-11.8	-9.5	9.1	3.7	9.7	0.0
Difference LP (%)	-14.5	-11.1	6.1	7.4	12.9	3.2

TABLE VII. COMPARISONS OF MEASURED AND PREDICTED TEMPERATURES BY 3D FE MODEL UNDER FAULT CONDITION AT 2/3 LOAD

Temperature (°C)	End winding			Active winding		
	set2_ew	set1_ew	tf_ew	b1_slot	tf_slot	e2_slot
Measured	76	63	66	54	62	63
Predicted max	72	66	78	60	69	67
Predicted min	54	49	64	49	61	49
Difference	5	--	--	--	--	--
Difference (%)	6.6	--	--	--	--	--

C. One Turn SC with 3-phase Terminal SC at Full Load

At one turn SC with 3-phase terminal SC at full load, the eddy current loss in the rotor magnets is 23.7 W. The iron loss is 221.4W, while the initial copper loss at 20°C is 1043W.

The predicted temperature distribution in the same fault condition as described in section VI-B but with full load current

excited in the healthy phases is shown in Fig. 14. As can be seen, the temperature distributions in the two healthy 3-phase sets are also similar while their overall temperatures are much higher than that of the faulty set which is consistent with the temperature distribution in the LP model. In this case, the hotspot is located in the middle part of the end winding of the healthy 3-phase sets, similar to those seen in Fig. 11, because of the much larger copper loss in the healthy phase sets. Table VIII compares the steady state average temperatures obtained by the predictions and measurements. It is of particular interest to note that the temperature in the coil with the fault is much lower than the temperature in the healthy phases with the application of the mitigation action although the current in the faulted turn is ~2.1 pu. This is because the total copper loss of the faulty 3-phase set is 3.5 times lower than that in the healthy 3-phase sets.

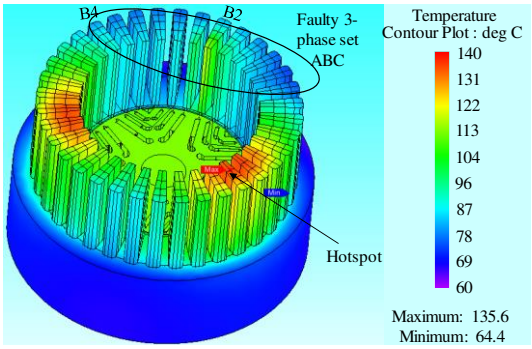

Fig. 14. Temperature distribution under fault condition at full load.

Table VIII shows that the differences between the measured and predicted average results by FE and LP models are largest at set2_ew with the values of 13.3% and 22.4%, while within 14.6% and 18.0% at five other sensors.

Table IX shows that the measured temperatures by the sensors denoted as set1_ew, tf_ew, b1_slot and e2_slot are between the minimum and maximum predicted temperatures in FE model. The measured temperature by sensor set2_ew is larger than the maximum predicted temperature by 5.6%, while the measured temperature by sensor tf_slot is 2.2% lower than the minimum predicted temperature.

It is evident that in three different conditions, the measured temperatures by sensor set2_ew are all quite larger than predicted average temperatures by LP and FE models, and even high larger than the maximum predicted results by 3D FE model. Moreover, from Table IV under healthy condition, the measured temperature by sensor set2_ew in the end winding region of the DEF set is larger than that by sensor set1_ew in the end winding region of the ABC set. This may be due to the fact that the sensor position in the DEF set is close to the star-neutral connection which brings extra resistance and loss, and hence higher temperature. Apart from the temperature at sensor set2_ew, the differences of average temperatures at five other sensors between 3D FE thermal models and the measurements are within 14.6%, while between 3D LP thermal models and the measurements are within 18.0%, according to Tables IV, VI, VIII.

TABLE VIII. COMPARISONS OF MEASURED AND PREDICTED AVERAGE TEMPERATURES UNDER FAULT CONDITION AT FULL LOAD

Temperature (°C)	End winding			Active winding		
	set2_ew	set1_ew	tf_ew	b1_slot	tf_slot	e2_slot
Measured	143	91	97	75	89	107
Predicted FE model	124	85	108	83	102	113
Predicted LP model	111	82	105	86	105	111
Difference FE (%)	-13.3	-6.6	11.3	10.7	14.6	5.6
Difference LP (%)	-22.4	-9.9	8.2	14.7	18.0	3.7

TABLE IX. COMPARISONS OF MEASURED AND PREDICTED TEMPERATURES BY 3D FE MODEL UNDER FAULT CONDITION AT FULL LOAD

Temperature (°C)	End winding			Active winding		
	set2_ew	set1_ew	tf_ew	b1_slot	tf_slot	e2_slot
Measured	143	91	97	75	89	107
Predicted max	135	99	117	91	104	123
Predicted min	92	72	95	73	90	78
Difference	8	--	--	--	-2	--
Difference (%)	5.6	--	--	--	-2.2	--

This is because that the sensor measures the temperature of one node of a region in which the maximum and minimum temperatures vary much and may have slightly large difference with the average temperature. Therefore, Tables V, VII and IX which compare the minimum and maximum temperatures of the same region predicted by the 3D FE thermal models with the measured results are more practical. It is obvious that the temperature differences at five other sensors between 3D FE thermal models and the measurements are within 6.3% from Tables V, VII and IX which are very close.

The comparisons of the predictions and measurements under both the healthy and fault conditions demonstrate that the 3D LP and 3D FE thermal models are reasonably accurate to predict temperatures with uneven loss distribution. However, due to the limited discretization level of the LP model, the FE model could provide more detailed temperatures of more different regions, such as active and end windings. Moreover, the 3D FE model could provide more clear temperature distribution and hotspot temperature which is significant in thermal analysis.

In addition, the consistency between the predictions and measurements further verifies that the machine can tolerant the worst case SC fault thermally with the mitigation action.

VII. CONCLUSION

A novel transient 3D LP thermal model and 3D FE thermal model for predicting asymmetric temperature distributions in a triple redundant, 9-phase PMASynRM under fault conditions have been established. It has been shown that both the steady-state and transient temperatures of the machine under SC fault conditions predicted by the LP thermal model agree well with those predicted by the FE thermal model. Moreover, the predicted machine temperatures by the LP and FE thermal models considering more realistic issues under healthy and fault conditions match well with the measurements. It can be concluded that both models could accurately predict asymmetric temperature distributions under faults.

In addition, these two models have high discretization level and are flexible for accounting practical issues, such as variable and uneven copper loss with the winding temperature, non-uniform end winding layout, and the time-varying coolant

temperature and flow rate, etc. The LP thermal model is easy to build, takes much less time and can predict accurately the average temperatures of different parts, especially the SC turn. The FE thermal model is more complex to build but it not only gives more detailed and clear temperature distribution of all parts but also estimates the hotspot temperature which is vital under thermal analysis. The LP model would be more suitable for thermal assessment of the fault tolerant machine in design stages while the FE model will be more accurate for thermal assessments in real operations.

REFERENCES

[1] B. Wang, J. Wang, B. Sen, A. Griffo, Z. Sun, and E. Chong, "A fault-tolerant machine drive based on permanent magnet-assisted synchronous reluctance machine," *IEEE Trans. Ind. Appl.*, vol. 54, no. 2, pp. 1349–1359, Mar./Apr.2018.

[2] A. Boglietti, A. Cavagnino, M. Lazzari, and M. Pastorelli, "A simplified thermal model for variable-speed self-cooled industrial induction motor," *IEEE Trans. Ind. Appl*., vol. 39, no. 4, pp. 945–952, Jul./Aug. 2003.

[3] A. Boglietti, A. Cavagnino, and D. A. Staton, "Determination of critical parameters in electrical machine thermal models," *IEEE Trans. Ind. Appl.*, vol. 44, no. 4, pp. 1150–1159, Jul./Aug. 2008.

[4] J. Wang, W. Wang, K. Atallah, and D. Howe, "Design of a linear permanent magnet motor for active vehicle suspension," *IEEE International Electric Machines and Drives Conference (IEMDC'09)*, pp. 585-591, Miami, FL, USA, May. 2009.

[5] D. Howey, A. Holmes, and K. Pullen, "Measurement and CFD prediction of heat transfer in air-cooled disc-type electrical machines," *IEEE Trans. Ind. Appl.*, vol. 47, no. 4, pp. 1716–1723, July-Aug. 2011.

[6] M. Galea, C. Gerada, T. Raminosoa, and P. Wheeler, "A thermal improvement technique for the phase windings of electrical machines," *IEEE Trans. Ind. Appl*., vol. 48, no. 1, pp. 79-87, Jan./Feb. 2012.

[7] X. Sun, M. Cheng, S. Zhu, and J. Zhang, "Coupled electromagnetic-thermal-mechanical analysis for accurate prediction of dual-mechanical-port machine performance," *IEEE Trans. Ind. Appl.*, vol. 48, no. 6, pp. 2240-2248, Nov/Dec. 2012.

[8] W. Jiang, and T. M. Jahns, "Coupled electromagnetic–thermal analysis of electric machines including transient operation based on finite-element techniques," *IEEE Trans. Ind. Appl.*, vol. 51, no. 2, pp. 1880-1889, Mar/Apr. 2015.

[9] G. J. Li, J. Ojeda, E. Hoang, and M. Gabsi. "Thermal-electromagnetic analysis of a fault-tolerant dual-star flux-switching permanent magnet motor for critical applications," *IET Electr. Power Appl.,* vol. 5, no. 10, pp. 503-513, Jul.2011.

[10] M. Manana, A. Arroyo, A. Ortiz, C. Renedo, S. Perez, and F. Delgado, "Field winding fault diagnosis in DC motors during manufacturing using thermal monitoring," *Applied Thermal Engineering*, vol. 31, no. 5, pp. 978-983, Apr. 2011.

[11] A. Sarikhani and O. A. Mohammed, "Inter-turn fault detection in PM synchronous machines by physics-based back electromotive force estimation," *IEEE Trans. Ind. Electron.*, vol. 60, no. 8, pp. 3472-3484, Aug.2013.

[12] Y. Shi, J. Wang, and B. Wang, "Lumped-parameter and 3D thermal model of a PMASynRM under fault conditions with asymmetric temperature distribution," *2018 IEEE Energy Convers. Congr. Expo. ECCE 2018,* pp. 6521–6528, Portland, Oregon, USA, Sept. 2018.

[13] A. K. M. Arafat, J. Herbert, M. T. Bin Tarek, and S. Choi, "Study of the thermal effects of a five-phase permanent magnet assisted synchronous reluctance motor under fault tolerant control," *2017 IEEE Int. Electr. Mach. Drives Conf. IEMDC 2017*, pp. 1–6, Miami, FL, USA, May. 2017.

[14] Y. Shi and J. Wang, "Continuous demagnetization assessment for triple redundant nine-phase fault-tolerant permanent magnet machine," *J. Eng*., vol. 2019, no. 17, pp. 4359–4363, Jun. 2019.

[15] B. Wang, J. Wang, A. Griffo, and B. Sen, "Experimental assessments of a triple redundant nine-phase fault-tolerant PMA SynRM drive", *IEEE Trans. Ind. Electron*, vol. 66, no. 1, pp. 772-783, Jan. 2019.

[16] Y. Shi, J. Wang, and B. Wang, "Performance assessment of triple redundant nine-phase delta- and wye-connected permanent magnet-assisted synchronous reluctance motor under healthy and fault conditions," *J. Eng*., vol. 2019, no. 17, pp. 3563–3567, Jun. 2019.

[17] Motor-CAD. [Online]. Available: www.motor-design.com.

[18] Z. Hashin and S. Shtrikman, "A variational approach to the theory of the effective magnetic permeability of multiphase materials," *Journal of applied Physics*, vol. 33, no. 10, pp. 3125–3131, Oct. 1962.

[19] N. Simpson, R. Wrobel, and P. H. Mellor, "Estimation of equivalent thermal parameters of impregnated electrical windings," *IEEE Trans. Ind. Appl.*, vol. 49, no. 6, pp. 2505–2515, Nov/Dec. 2013.

[20] L. Idoughi, X. Mininger, F. Bouillault, L. Bernard, and E. Hoang, "Thermal model with winding homogenization and FIT discretization for stator slot," *IEEE Trans. Magn.*, vol. 47, no. 12, pp. 4822–4826, Dec. 2011.

[21] JMAG. [Online]. Available: www.jmag-international.com.

[22] D. P. Kulkarni, G. Rupertus, and E. Chen, "Experimental investigation of contact resistance for water cooled jacket for electric motors and generators," *IEEE Trans. Energy Convers.*, vol. 27, no. 1, pp. 204–210, Mar. 2012.

[23] S. Xue, W. Q. Chu, Z. Q. Zhu, J. Peng, S. Guo, and J. Feng, "Iron loss calculation considering temperature influence in non-oriented steel laminations," *IET Sci. Meas. & Tech*., vol. 10, no. 8, pp. 846–854, Nov. 2016.